CHALMERS

CHALMERS
UNIVERSITY OF TECHNOLOGY

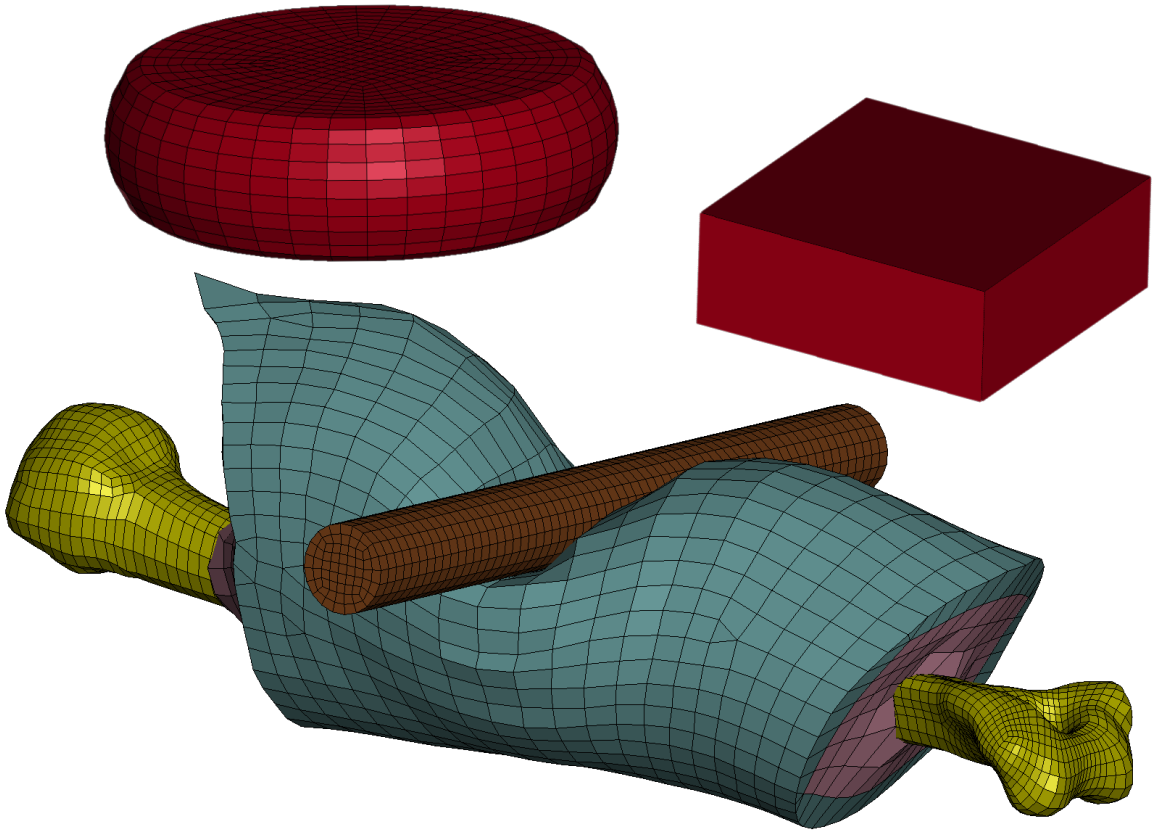

Student Thesis – Mechanics and Maritime Sciences (M2) – Project Work

Finite Element Calibration of Muscle for Human Body Models

TME131 Project in Applied Mechanics 2025

Department of Mechanics and Maritime Sciences
CHALMERS UNIVERSITY OF TECHNOLOGY
Gothenburg, Sweden 2025

Finite Element Calibration of Muscle for Human Body Models

TME131 Project in Applied Mechanics 2025

Student Thesis – Mechanics and Maritime Sciences (M2) – Project Work

Project in Applied Mechanics TME131, 2025
Department of Mechanic and Maritime Sciences
Chalmers University of Technology
SE-412 96 Gothenburg
Telephone +46 31 772 1000

Cover: Unit Cell Test (upper left), Single Element Test (upper right), Humerus Bar Impact Test from SAFER (bottom).

Typeset in LaTeX
Gothenburg, Sweden 2025

Preface

The work in the present report was carried out as a part of the course TME131 Project in Applied Mechanics, which is a mandatory course within the Applied Mechanics Masters programme at Chalmers. The course was carried out during spring semester 2025. The project was supervised by: Johan Iraeus, Department Mechanic and Maritime Sciences
Jobin John, Department of Mechanics and Maritime Sciences

Abstract

Accurate modelling of muscle tissue is critical for realistic human body simulations in biomechanics and vehicle safety applications. This project focuses on calibrating and validating visco-hyperelastic material models for muscle tissue, specifically comparing the Ogden model and a General Hyper-elastic rubber model, implemented in LS-DYNA. The study leverages uniaxial compression test data at strain rates ranging from quasi-static (0.01/s) to dynamic (90/s) to fit material parameters. Analytical derivations and numerical optimizations (using LS-OPT) were employed to calibrate the models, followed by validation via Single-Element Tests and Unit Cell Tests to assess stability and accuracy.

Results demonstrate that the Ogden model effectively captures quasi-static and low strain-rate behaviour but exhibits discrepancies in visco-elastic regimes, overestimating stresses at higher strains and strain-rates. The General Hyper-elastic model provided a comparable fit but required higher-order terms for accuracy. Both models achieved numerical stability close to 70% compressive strain, benchmarked against a material implementation known to be numerically stable. Full-scale impact simulations using the SAFER Human Body Model revealed close alignment with experimental data for humerus plate impacts, though deviations occurred in bar impact scenarios.

Key challenges included interpreting LS-DYNA's visco-elastic implementation. Future work should address viscous behaviour modelling, expand experimental datasets, and refine geometry-specific calibrations. This study advances the fidelity of muscle tissue representation in HBMs, supporting safer automotive design and injury prediction.

Acknowledgements

We would like to express our gratitude to our supervisors, Johan Iraeus and Jobin John, for the support, guidance, and dedication throughout the course of this project. They played a central role in helping us shape the direction of our work, offering technical insight and critical feedback at every stage of the process.

A special thanks to the access of the SAFER HBM models.

From the initial planning to the final validation, Johan and Jobin was consistently involved, providing suggestions for improvement, and ensuring the quality and clarity of our results. Their willingness to meet regularly and offer constructive advice greatly enhanced the learning experience and contributed significantly to the final outcome of this study. We are especially thankful for the time and effort they invested in reviewing our simulations, checking the consistency of our methodology, and helping us interpret the results in a meaningful way. The project benefited enormously from their expertise and commitment.

Without this guidance, the successful completion of this work would not have been possible. In the process of writing and editing this report, we also made use of AI-based tools such as ChatGPT [1] and DeepL [2]. These tools were used to support grammar correction, improve sentence clarity, and ensure cohesion throughout the report.

Contents

1

Introduction

Accurate modelling of muscle tissue is essential for realistic human body simulations. This report focuses on the improvement of existing material models currently available for use in human body models (HBM), one such HBM is the open-source framework VIVA+ VivaPlus [3]. The report presents an evaluation of the model's implementation, both analytically and in simulation environments. A comparative analysis of these models is conducted, with the objective of ascertaining the most suitable model based on optimisation results. Furthermore, if applicable, the reasons for any discrepancies between the models are investigated and potential avenues for future analysis are discussed in order to support further development based on the findings of this report.

1.1 Background

Prior to the advent of the well-known Anthropomorphic Test Devices (ATDs), more commonly referred to as "crash test dummies", the practice in Vehicle Occupant Safety (VOS) testing entailed the utilisation of cadavers, chimpanzees, hogs, and other animals for physical testing purposes [4]. This approach is documented in the research publication by Pan et al. [4]. The financial and ethical[1] implications of conducting physical tests, in conjunction with accelerated iterative cycles of product evaluation, more intricate loading scenarios, and technological advancements in computing, have prompted the utilisation of mathematical models to assess crashworthiness. Advancements in this field have included the development of virtual occupant surrogates, such as the ATDs employed in physical testing, as well as full Human Body Models (HBMs). The aforementioned constructs are of a mathematical nature, and their purpose is to facilitate the evaluation of the influence of different scenarios without the necessity of conducting physical tests. As illustrated in Fig. 1.1, a virtual occupant surrogate in the form of an HBM is presented.

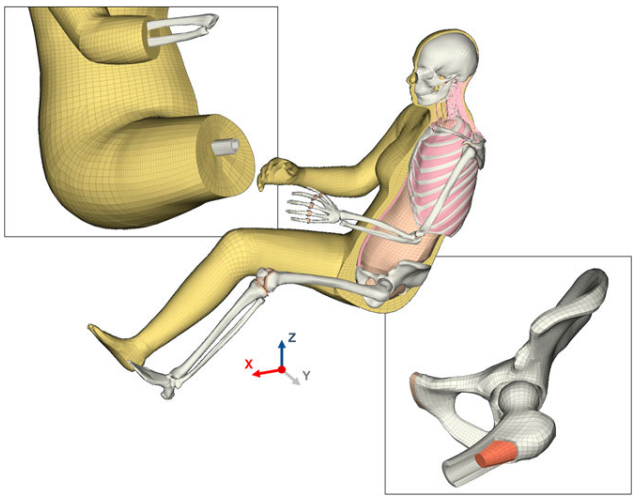

Fig. 1.1: FE-model of the VIVA+ base model. In the center, the full HBM is shown with half being complete and half without soft-tissue. Top left image shows the mesh of the soft-tissue close up while the bottom right shows the mesh of the hipbone and a part of the femur. Image is reused from [5] under Creative Commons Attribution License.

[1]Ethical implication when it comes to animal and cadaver testing.

The Cambridge Dictionary defines biomechanics as 'the physical forces that affect human and animal movement, or the study of these forces' [6]. The utilisation of HBMs facilitates the capture of the biomechanics of the human body under varying loads. In the context of VOS, short transient events are of particular interest. This is evidenced by the occurrence of such events in different types of accidents, including collisions and rollover events. Pipkorn et al. [7] provide a detailed discussion of the evaluation of occupant protection systems, including seat belts and airbags, through the utilisation of crash tests that employ ATDs. These devices estimate injury risk based on global injury criteria, such as chest deflection to estimate thorax injuries. However, the authors highlight the limitations of anthropomorphic test devices (ATDs), particularly their reduced biofidelity and restriction to specific impact directions. To overcome these shortcomings, finite element (FE) HBMs are emphasized for their ability to predict injuries omnidirectionally and to represent human anatomy in greater detail. As a result, FE-HBMs enable injury risk assessments at the tissue level, allowing for more precise evaluation of injury mechanisms.

The modelling of human soft tissue poses a considerable challenge due to the complex mechanical characteristics it exhibits. Soft tissues are characterised by a high degree of softness, an absence of compressibility, and a notable level of rate dependence, a behaviour typically associated with viscoelasticity. It is also noteworthy that the subject of whether soft tissue is compressible or not is a matter of ongoing discussion in the relevant literature, as referenced in the work of Chavan [8]. Furthermore, the material shows non-linear behaviour, as observed in the same source, it has been demonstrated that these properties frequently result in numerical challenges when employing the Finite Elements Method (FEM) primarily due to mesh distortion under large deformations and volumetric locking associated with a nearly incompressible material model that enforces incompressibility [9]. In this study, an Ogden-based hyper-elastic material model was used to describe the non-linear stress–strain behaviour of soft biological tissue. The task was to fit this model to experimental data and evaluate its performance. As part of the assigned task, the Ogden model, a widely used constitutive model for soft materials, was employed to assess its suitability for representing viscoelastic biological tissue.

1.2 Purpose

The purpose of this project is to implement and validate material parameters for muscle tissue using visco-hyperelastic models based on two material model formulations. The first is the Ogden model which has been extended to include rate-dependent behaviour to account for the viscoelastic nature of muscle tissue under different strain rates. The second is the general hyper-elastic material model formulation extended with a viscoelastic formulation.

The experimental data utilised for parameter fitting comprises uniaxial compression tests performed on human specimens at various strain rates. The implementation of such tests enables the acquisition of stress-strain curves across a range of loading velocities, thereby facilitating the discernment of quasi-static and dynamic material responses. The material parameters are estimated using this data, including additional rate-dependent terms to account for strain rate effects.

Subsequent to validation, the fitted parameters are applied in full-scale impact simulations using a HBM in the LS-DYNA FE-software. The stability of the muscle elements is assessed and benchmarked against adipose tissue in order to ensure consistency in the strain range across soft tissues.

In addition to the implementation of parameters, the project involves the further devel-

opment of the understanding of hyper-elastic and visco-elastic modelling techniques within the field of biomechanics. The programme encompasses practical learning of LS-DYNA and a critical evaluation of the simulation's capability to match experimental data.

1.3 Aim

The aim of this project is to calibrate Ogden material parameters using uniaxial compression experimental data and assess their impact on element stability in LS-DYNA simulations, with the goal of enabling their use in a full human body model (HBM) simulation. While not a primary aim of the project, a general hyper-elastic material model was also implemented for comparison with the Ogden-based model, in order to evaluate differences, similarities, and potential limitations between the two formulations.

2

Theory

The two models analysed in this study are based on hyper-elastic strain energy functions, augmented with a linear viscoelastic time-dependent response, as described in the LS-DYNA Keyword User's Manual [10]. The inclusion of visco-elasticity accounts for rate-dependent mechanical behaviour, which is critical for modelling biological tissues under dynamic loading. The material parameters are calibrated against experimental data from a uniaxial compressive test [11]. Consequently, the analytical derivations are also conducted under uniaxial deformation. For simplicity, an incompressibility assumption is applied. This simplification is justified for soft tissues, where volumetric stiffness significantly exceeds shear stiffness [10].

2.1 Ogden Hyper-elastic Material Model

The Ogden material model is implemented based on a hyper-elastic strain energy density function (Eq. 2.2), where volumetric effects are decoupled by expressing the principal stretches in isochoric form [10].

$$\lambda_i^* = \frac{\lambda_i}{J^{1/3}}, \quad \text{with } J = \lambda_1\lambda_2\lambda_3 \tag{2.1}$$

The strain energy density function takes the form:

$$W = \sum_{i=1}^{3}\sum_{j=1}^{n} \frac{\mu_j}{\alpha_j}\left(\lambda_i^{*\alpha_j} - 1\right) + K\left(J - 1 - \ln J\right) \tag{2.2}$$

Here, n denotes the number of Ogden terms (model order), μ_j and α_j are material parameters and K is the bulk modulus, enforcing near-incompressibility via a penalty term to penalize volumetric changes [10].

The bulk modulus is related to the shear moduli and Poisson's ratio through:

$$K = \frac{2\mu}{3(1-\nu)}, \quad \text{with } \mu = \sum_{j=1}^{n}\mu_j \tag{2.3}$$

The principal Kirchhoff stresses are derived from the strain energy function and tranformed using the eigenvector matrix $\mathbf{q}$ as [12]:

$$\tau_{ii}^E = \lambda_i \frac{\partial W}{\partial \lambda_i} \implies \tau_{ij} = q_{ik}q_{jl}\tau_{kk}^E \tag{2.4}$$

For uniaxial loading, the deformation occurs along a principal axis, simplifying the transformation to the identity:

$$q_{ij} = \delta_{ij} \implies \tau_{ij} = \tau_{ij}^E \tag{2.5}$$

The Cauchy stress is then obtained by volume normalization, where for an incompressible material ($J = 1$):

$$\sigma_{ij} = J^{-1}\tau_{ij} \implies \lambda_i \frac{\partial W}{\partial \lambda_i} \tag{2.6}$$

Under uniaxial deformation, the Cauchy stress for the Ogden model simplifies to:

$$\sigma_{11} = \sum_{i=1}^{n} \mu_i \left(\lambda^{\alpha_i} - \lambda^{-\alpha_i/2}\right) \tag{2.7}$$

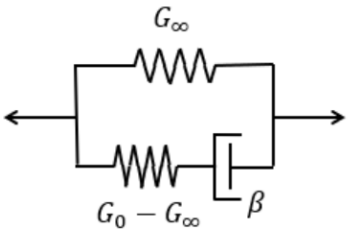

$$G(t) = G_\infty + (G_0 - G_\infty)\exp(-\beta t)$$

Fig. 2.1: Standard visco elastic Model: Spring and Maxwell element in parallel.

2.2 General Hyper-elastic Rubber Material Model

Similar to the Ogden model discussed in Section 2.1, the Cauchy stress for a General Hyper-elastic material is derived from a strain energy density function. The formulation used in this work follows the general polynomial model as described in the *LS-DYNA Theory Manual* [12], and is expressed in Eq. 2.8:

$$W = \sum_{p,q=0}^{n} C_{pq} W_1^p W_2^q + \frac{1}{2}K(J-1)^2, \tag{2.8}$$
$$\text{with:} \quad W_1 = I_1 I_3^{-1/3} - 3, \quad W_2 = I_2 I_3^{-2/3} - 3$$

Here, C_{pq} are material parameters, K is the bulk modulus, and I_1 and I_2 are the first and second invariants of the right Cauchy-Green deformation tensor, respectively. The third invariant $I_3 = \det(\mathbf{C}) = J^2$ is associated with volumetric deformations. Under the assumption of incompressibility, $J = 1$, implying $I_3 = 1$.

The procedure for computing the Cauchy stress mirrors that used for the Ogden model, where the stress is derived from the strain energy function using:

$$\sigma_{ij} = \lambda_i \frac{\partial W}{\partial \lambda_i} \tag{2.9}$$

Applying this formulation to the general polynomial strain energy function under uniaxial loading yields the final expression for the Cauchy stress:

$$\sigma_{11} = \lambda \frac{d}{d\lambda} \left(\sum_{p,q=0}^{n} C_{pq} \left(\lambda^2 + 2\lambda^{-1} - 3\right)^p \left(2\lambda + \lambda^{-2} - 3\right)^q \right) \tag{2.10}$$

2.3 Visco-elastic Stress

According to [13], strain rate effects are taken into account through linear visco-elasticity by a convolution integral of the form:

$$\sigma_{ij}^v = \int_0^t G_{ijkl}(t-\tau) \frac{\partial \epsilon_{kl}}{\partial \tau} d\tau \tag{2.11}$$

This model is effectively a Maxwell fluid which consists of dampers and springs in series according to the standard viscoelastic model seen in Fig. 2.1

This implementation results in a visco-elastic stress contribution, where $G(t)$ equals relaxation functions for corresponding stress measures, defined for relaxation times $\tau_i = \frac{1}{\beta_i}$ $[s]$ as:

$$G(t) = G_\infty + \sum_{i=1}^{N} G_i \, e^{-t/\tau_i} \tag{2.12}$$

In order to derive a explicit stress update scheme suitable for analytical implementation, the procedure provided in [14] was used. Resulting in a explicit stress update scheme at time step k and for n Maxwell elements using normalized relaxation functions g_i:

$$\sigma^k = \sigma_\infty^k + \sigma^{v,k} \quad \text{where } \sigma^{v,k} = \sum_{i=1}^{n} \sigma_i^k = \sum_{i=1}^{n} g_i e^{-t^k/\tau_i} \sum_{l=2}^{k} e^{-t^k/\tau_i} (\sigma_e^l - \sigma_e^{l-1}) \tag{2.13}$$

Here σ_∞^k is the evolution of the relaxed instantaneous elastic stress according the material up to time t^k, calculated as:

$$\sigma_\infty^k = g_\infty \sum_{l=2}^{k} (\sigma_e^l - \sigma_e^{l-1}) \tag{2.14}$$

Where σ_e is the instantaneous material specific stress response according to 2.1 and 2.2. For the implementation time step $l = 1$ is omitted and arbitrary set to zero for initialization. Where the long-term modulus G_∞ is retrieved from the quasi static material calibration. From curve fitting under different strain rates according to above stress evolution, we obtain the dimensionless Prony coefficients g_i. These coefficients are defined as:

$$g_i = \frac{G_i}{G_0}, \quad \text{where} \quad G_0 = G_\infty + \sum_{i=1}^{N} G_i \tag{2.15}$$

Where the normalized long-term modulus is:

$$g_\infty = \frac{G_\infty}{G_0} = 1 - \sum_{i=1}^{N} g_i \tag{2.16}$$

Solving for the instantaneous modulus G_0:

$$G_0 = \frac{G_\infty}{g_\infty} = \frac{G_\infty}{1 - \sum g_i} \tag{2.17}$$

Then, each dimensional modulus G_i can be recovered as:

$$G_i = g_i \cdot G_0 = g_i \cdot \frac{G_\infty}{1 - \sum g_i} \tag{2.18}$$

It is thus possible, using this procedure, to fit the material response at different strain rates by using either absolute or normalized relaxation moduli, as controlled by the LS-DYNA parameter *VFLAG*. This choice influences how the viscoelastic response is interpreted during simulation: using normalized moduli ensures that the total relaxation scales with the instantaneous modulus, while absolute values specify fixed relaxation behavior regardless of the initial stiffness. Depending on the selected approach, this can significantly affect how accurately the model captures rate-dependent effects, especially when calibrating across multiple strain rates.

3

Method

The overall procedure followed in this study is summarised in Fig. 3.1, which presents the key steps undertaken to achieve the project's objective.

In the initial phase of the analytical calculations, the preliminary parameters for the shear moduli, denoted by μ_i, and the strain hardening parameters, denoted by α_i, for the first- and second-order Ogden models were utilised. The calibration of these parameters was achieved through the use of curve fitting, a statistical analysis technique, applied to experimental data obtained from uniaxial compression tests of muscle tissue under quasi-static conditions (engineering strain rate of 0.01/s). It is noteworthy that the engineering strain levels only up to a maximum of 50% was used for the parameter fitting, as outlined in the literature on muscle testing [11].

The material model was then applied to a single finite element in LS-DYNA, which was subjected to the same loading conditions, in terms of engineering strain rates and total strains, as those used in a benchmark model for adipose tissue. Furthermore, a General Hyper-elastic material model was implemented and fitted to the experimental data in a similar manner. The implementation of both models enabled a comparison of the performance of the Ogden and General Hyper-elastic formulations. In the subsequent phases of the analysis, a visco-elastic component was integrated into both models to encapsulate time-dependent effects and further enhance their congruence with the observed behaviour.

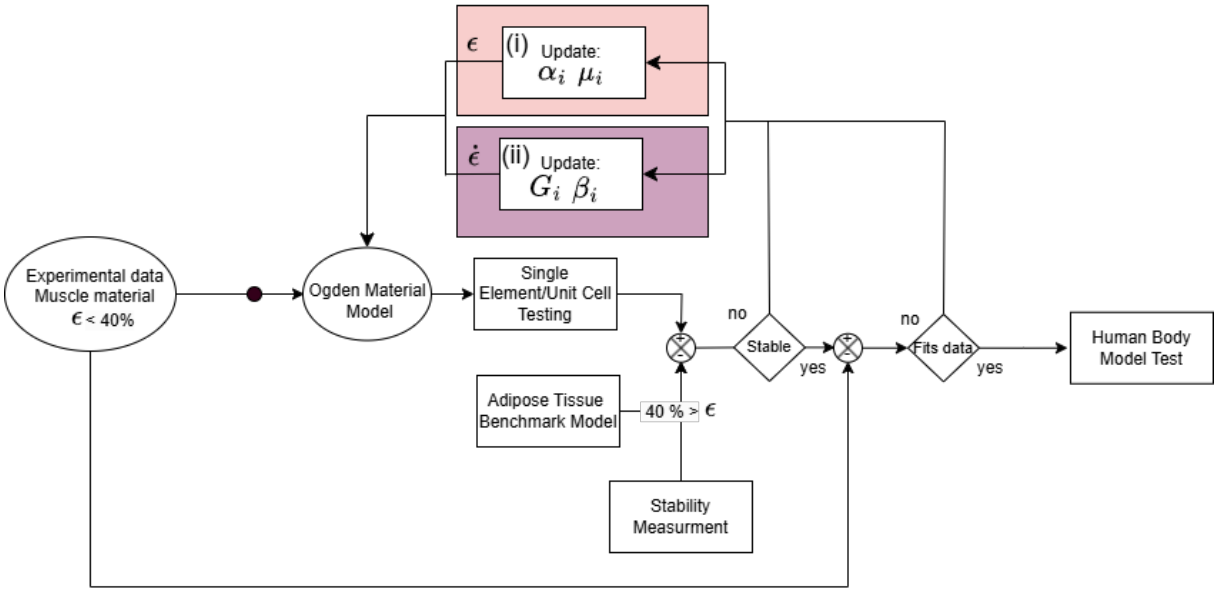

Fig. 3.1: A schematic of the project procedure.

The model parameters α_i, μ_i, G_i, and β_i for the Ogden model were iteratively adjusted to:

1. *Increase the maximum ultimate strain before the model becomes unstable.*
2. *Sustain the model's asymptotic behavior in agreement with the experimental data in the low strain region ($\epsilon < 40\%$).*

Furthermore, the optimized material models were implemented in a Unit Cell Test to evaluate their stability and to benchmark them against the adipose tissue model provided

by [15], with the intention of subsequently applying them in a full-scale Human Body Model (HBM) simulation. The same procedure was followed for the General Hyper-elastic model, using its respective material constants.

3.1 Material Model Calibration

The calibration of the material model is a multi-step process, the details of which are outlined in the subsections that follow. This process is imperative to ensure that the material behaviour is accurately represented and that the model implementations are correct. The calibration process entailed the adjustment of material parameters to align with experimental data derived from tests conducted on human muscle tissue. Specifically, LS-OPT was utilised to optimise the material parameters numerically by fitting the experimental data to the stress–strain response of a numerical Single-Element Test (SET).

The analytical results obtained were utilised to provide initial parameter estimates for the optimisation process in LS-OPT. The parameters obtained through this method corresponded directly to the response of a single element model implemented in LS-DYNA. Subsequently, these parameters were verified and further refined through numerical calibration using LS-OPT and validated using both SET and Unit Cell Tests (UCT).

3.1.1 Analytical Calibration

The material models were calibrated using experimental data obtained from human muscle tissue, as previously mentioned (MuscleTest). The engineering stress and strain values were extracted from the experimental dataset, and the corresponding stretch ratios (λ) were calculated from the engineering strain values using the relation: $\lambda = 1 + \varepsilon$.

The implementation of the constitutive equations for the two hyper-elastic models – the General Hyper-elastic Rubber model and the Ogden Rubber model – was then achieved by utilising the stretch values. These models are described in Chapter 2. The calibration process was initiated with an initial estimate for the model parameters.

Subsequently, the model parameters were optimized by minimizing the sum of squared differences between the calculated and experimental engineering stress values. This sum represented the total error, which was minimised using the Generalised Reduced Gradient (GRG) method, implemented via Excel's Solver tool. The GRG method is an iterative optimization algorithm that adjusts model parameters while ensuring active constraints are respected throughout the process [16].

Initial calibration was conducted for the quasi-static condition (strain rate of 0.01/s), which was then utilised as the baseline for further analysis. In the subsequent phases of the modelling process, visco-elastic terms were incorporated with the objective of accounting for time-dependent behaviour. The same overall curve-fitting approach was applied to both the quasi-static and rate-dependent cases, wherein analytical stress–strain expressions were fitted to experimental data by minimizing the error to determine optimized material parameters.

3.1.2 Numerical Calibration: LS-OPT

In accordance with the SET that will be introduced in Section 3.2.1, numerical material model calibration can be performed with the tool LS-OPT. This tool is a sophisticated programme that employs the LS-DYNA engine and its keycards to optimise parameters based on various criteria and optimisation methods.

The determination of the initial numerical material parameters was achieved through a comprehensive analysis of the analytical material parameters outlined in Chapter 2 and the viscous parameter range established by H. Naseri in [15].

The LS-OPT methodology was employed to ascertain whether the calibration of analytical material would yield the correct set of parameters, or whether a more optimal set could be identified via LS-OPT within the local range of the analytically predicted parameters. Furthermore, alternative material parameters could be identified to capture the material behaviour in different strain-rate ranges in order to bias the higher ranges.

The core components employed in LS-OPT comprised a polynomial metamodel utilising a linear order fitting with a point selection termed D-Optimal and domain reduction (SRSM) employing the default values. The composite definition employed was that of curve matching, whereby the test data were evaluated against the response values of the SET models integration point (see Section 3.2.1). Depending on the objective of the curve fitting, the parameters to be fitted, along with their initial guess, the parameters upper and lower bounds, simulation points, number of iterations and objective weights were all adjusted based on independent optimisation simulations.

3.2 Numerical Verification: Single-Element Test and Unit Cell Test

Based on the results of the analytical material calibration presented in Chapter 4.1, the material parameters were identified through curve fitting and subsequently implemented in LS-DYNA. This implementation aimed to verify whether the engineering stress–strain response predicted by the constitutive equations was consistent with the behavior observed in finite element simulations. In addition, it enabled validation of the parameters obtained using Excel's Solver tool and facilitated a direct comparison between the analytical and numerical stress–strain curves.

Two primary evaluation criteria were considered:

1. **Model Accuracy:** Assess whether the numerical results reproduce the experimental data and/or analytical solutions for each material model.

2. **Numerical Stability:** Ensure the numerical stability of the material model is comparable to the implementation of adipose tissue with average stiffness, as reported in [15], which remained stable under compressive strains up to approximately 70%.

To assess these criteria, two finite element model configurations were used:

- **Single-Element Test (SET):** Designed to evaluate the stress–strain response and examine volumetric effects that may impact numerical stability [17].
- **Unit Cell Test (UCT):** Developed to assess the stability of the material model in simulations involving multiple elements, ensuring no unexpected numerical artifacts arise.

All simulations were performed using LS-DYNA Unit System C [13], with units defined as millimeters (mm), milliseconds (ms), kilograms (kg), kilonewtons (kN), and gigapascals (GPa).

For both model configurations, 8-noded constant strain hexahedral elements (`ELFORM=1`) were employed. The time step scale factor (`TSSFAC`) was set to 0.7 for the SET to improve numerical robustness in high strain-rate conditions, as recommended in [17], while the default value of 0.9 was maintained for the UCT.

3.2.1 Single-Element Test

To evaluate the fundamental behaviour of the calibrated material models in a controlled environment, a SET was performed. This test allows for direct comparison between analytical and numerical stress–strain responses and provides insight into potential numerical issues such as volumetric locking or instability during large deformations. For stability, the volumetric change was suspected to be of importance [15], potentially leading to volumetric locking.

Given the theory in Chapter 2, LS-DYNA uses a near-incompressible formulation [10], which employs the volumetric scaling variable J to numerically implement near-incompressibility as defined in Chapter 2.1. When the volume deviated from its original state, numerical issues were observed in bodies composed of multiple elements. Therefore, the SET also served to assess whether numerical instability in the UCT (see Section 3.2.2) could be pre-emptively predicted through early signs of volumetric deviation. It also serves as a useful baseline before implementing the material in the UCT.

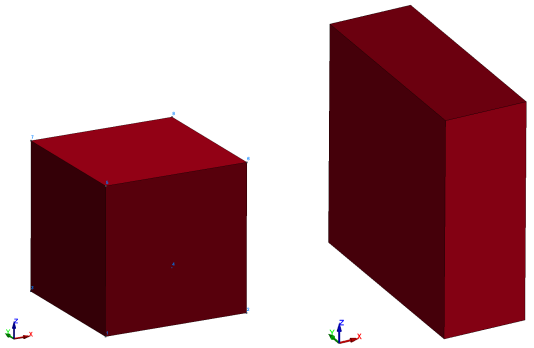

(a) Non-deformed. (b) Deformed.

Fig. 3.2: SET model under compressive load. Fig. 3.2a shows the base model, and Fig. 3.2b the deformed FE-model.

The SETs are based on the framework in [18], in accordance with a uniaxial compressive test. The element size used was 1x1 mm for all models. The engineering strain rate in the chosen unit system becomes:

$$\dot{\varepsilon}_x = \frac{\dot{u}_x}{l_0^{SET}} \left[\frac{1}{ms}\right], \tag{3.1}$$

where $l_0^{SET} = 1$ [mm] representing the x-length of the SET.

A schematic of the SET base model Fig. 3.2a and the effect of boundary conditions [18] while under compressive load (in the x-direction) are shown in Fig. 3.2b. The stress–strain values were evaluated at the element's integration point (using *DATABASE_ELOUT) to enable comparison between the SET results and the analytical solution presented in Section 2.

3.2.2 Unit Cell Test: Stability Evaluation

To evaluate the stability of the material model, a UCT was set up to correlate the model's behaviour with that of a benchmark material model [15].

The UCTs were inspired by the methodology in [18], but were modified to more accurately reflect the geometry of the physical test specimen described in [11]. The model is shown in Fig. 3.3, with the nodal sets for the top and bottom sides illustrated in Fig. 3.3a and Fig. 3.3b, respectively. The boundary conditions for the physical test were not fully defined in [11], due to uncertainty regarding friction between the compression tool and the specimen, two boundary condition cases were defined: an upper bound, where the nodes in Fig. 3.3 were fixed in the YZ-plane, and a lower bound, where they were free.

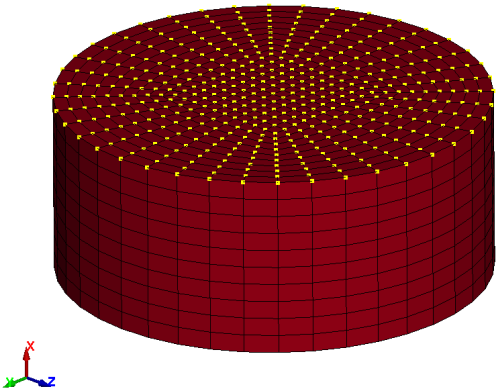

(a) Unit Cell's top node set.

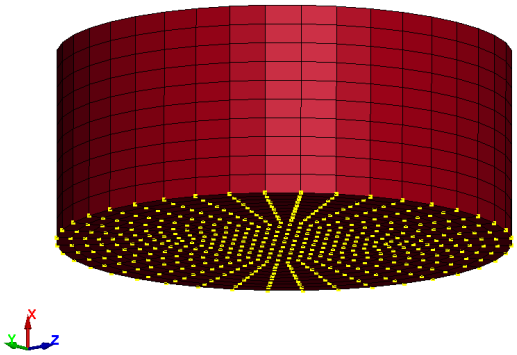

(b) Unit Cell's bottom node set.

Fig. 3.3: Illustration of the Unit Cell muscle model. The top and bottom nodal sets are shown in Fig. 3.3a and Fig. 3.3b, respectively.

In the simulations presented, an upper bound boundary condition was applied: both sets of nodes were constrained in the YZ-plane. The bottom side was fixed in the X-direction, while the top side was assigned a prescribed compressive velocity in the X-direction. This setup was intended to capture the model's barrelling behaviour, which resembles the actual response of the specimen under compression in physical tests. see Fig. 3.4.

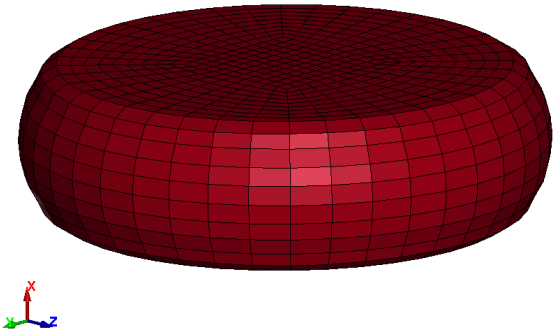

Fig. 3.4: Muscle Unit Cell model under compressive load.

The deformation of the muscle model under the applied boundary conditions is shown in Fig. 3.4, where it can be seen that expansion in the YZ-plane was fully restricted by the top and bottom constraints.

At high strain rates and large compressive strains, numerical instabilities could occur. Elements could become distorted, experience negative volumes, and/or exhibited nonphysical behavior, which eventually leads to termination of the LS-DYNA solver.

The strain average (over the elements) used to evaluate the stable range of deformation was calculated as:

$$\varepsilon_x = \frac{u_x}{l_0^{UC}}, \tag{3.2}$$

where $l_0^{UC} = 4$ mm is the initial length of the Unit Cell in the X-direction. The applied strain rate was defined as:

$$\dot{\varepsilon}_x = \frac{\dot{u}_x}{l_0^{UC}} = 90 \left[\frac{1}{\text{ms}}\right]. \tag{3.3}$$

3.3 HBM Benchmarking

To correlate the material model's response in a HBM, impact tests based on the SAFER [19] HBM FE-models was compared to experimental data from a corresponding physical impact test and to the adipose tissue material models from H. Naseri [15].

The adipose tissue was coloured cyan, while the part of the model where the muscle material model was implemented in the magenta-coloured component as shown in Fig. 3.5 and Fig. 3.6.

3.3.1 SAFER HBM: Humerus Plate Impact

A humerus plate impact test can be seen in Fig. 3.5 from SAFER [19]. The plate will have two different initial velocities,

$$\dot{u}_0^I = 2 \left[\frac{m}{s}\right], \ \dot{u}_0^{II} = 4 \left[\frac{m}{s}\right] \tag{3.4}$$

for the plate impact test. From Fig. 3.5a and Fig. 3.5b, the start of the simulation and during the impact is shown, respectively. For the comparison, the experimental data from A. Kemper [20] for the female specimens was used for the two initial velocities.

The response from the humerus model is measured as the reaction force in the Z-direction on the surface of the impactor, the brown plate in Fig. 3.6.

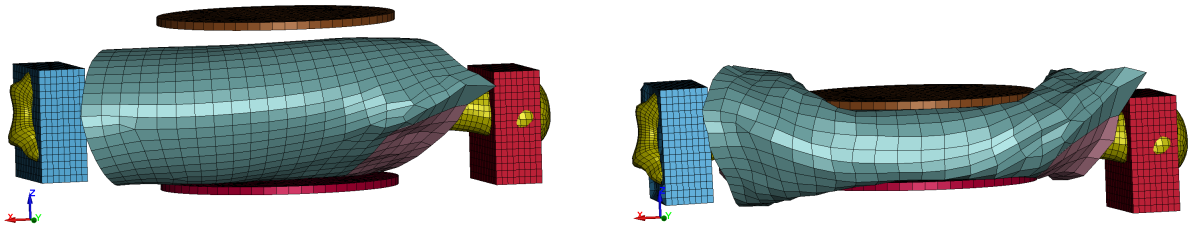

(a) SAFER Humerus model before plate impact.

(b) SAFER Humerus model during plate impact.

Fig. 3.5: Visualisation of humerus model during plate impact. Model from [19].

3.3.2 SAFER HBM: Humerus Bar Impact

For the humerus bar impact test shown in Fig. 3.6, the initial velocity of the bar was set to correspond with the experimental test conducted by S. Duma et al. [21], where the initial velocity is given as:

$$\dot{u}_0 = 3.63 \left[\frac{m}{s}\right], \tag{3.5}$$

in which they also provide the experimental force-time results on the humerus.

As shown in Fig. 3.6a and Fig. 3.6b, the start of the simulation and the impact phase are illustrated, respectively.

The response from the humerus model is measured as the reaction force in the Z-direction on the surface of the impactor, the brown rod in Fig. 3.6.

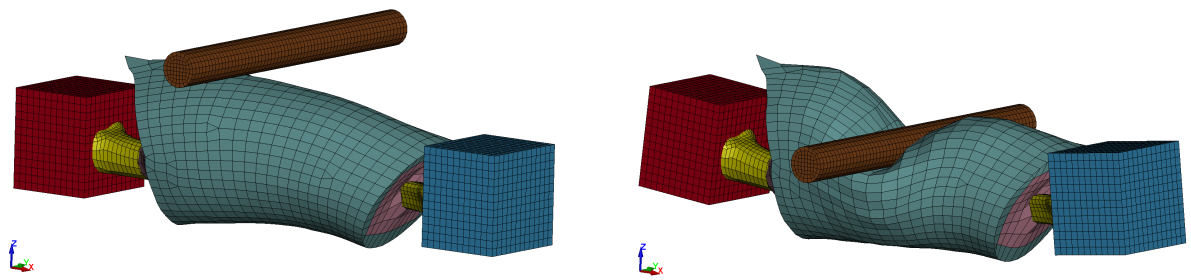

(a) SAFER Humerus model before bar impact.

(b) HBM setup during bar impact.

Fig. 3.6: Model before and after impact. Model from [19].

4

Results

This chapter presents the results from the calibration and validation of the muscle material model. It includes the quasi-static material response at low strain rates, the calibrated viscoelastic parameters for the General Hyper-elastic and Ogden models, and the outcome of parameter optimization using LS-OPT. Finally, the model performance is evaluated in impact simulations using the SAFER HBM framework.

4.1 Calibration and Validation Results for Quasi-Static Material Response (0.01/s)

The Ogden material model, calibrated using the optimised parameters obtained via Excel's Solver tool as seen in Section 3.1.1, for the first-, second-, and third-order formulations, are presented in Fig. 4.1a. The results showed that the first-order model was adequate, based on how closely the corresponding curves aligned (see Fig.4.1a). These parameters were subsequently validated against the first-order Ogden implementation in LS-DYNA using the SET, see Section 3.2.1. The validation results are illustrated in Fig. 4.1b.

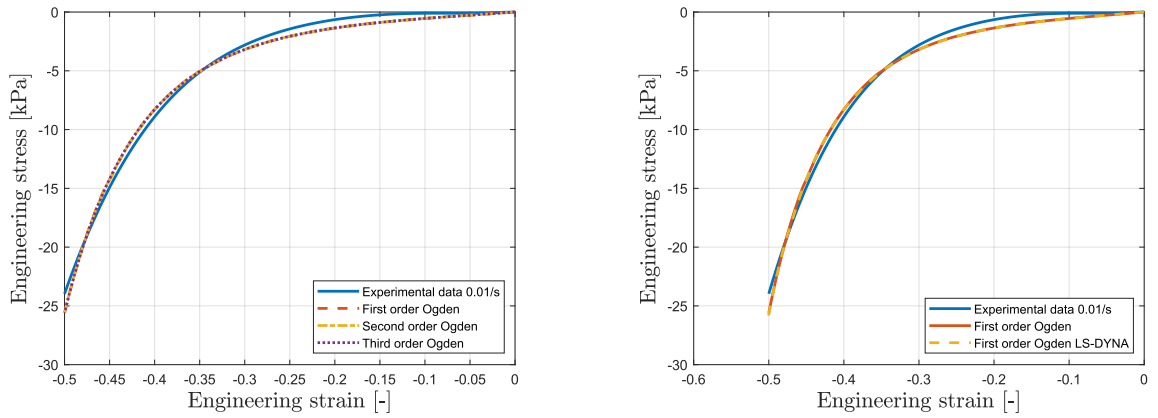

(a) Ogden models calibrated with experimental data

(b) Validation with LS-DYNA for Ogden material

Fig. 4.1: Comparison of Ogden model calibration and LS-DYNA validation

It can be observed that the various Ogden models, when calibrated with the optimised parameters, exhibited a high degree of correlation with the experimental data, with only minor deviations recorded. Moreover, the analytical solution was found to be identical to the corresponding LS-DYNA simulation results.

The results of the calibrated General Hyper-elastic material model, along with the experimental data for the quasi-static case, are presented in Fig. 4.2a.

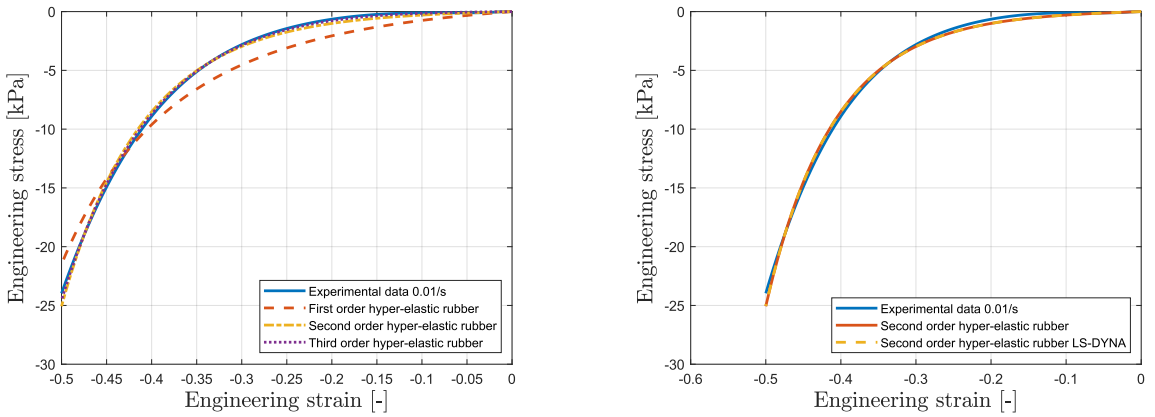

(a) Calibration of Hyper-elastic rubber (b) Validation of Hyper-elastic rubber model

Fig. 4.2: Calibration and validation results for the General Hyper-elastic rubber model

As demonstrated in Fig. 4.2a, the first-order model underestimates the material stiffness and deviates from the experimental response. The incorporation of the second-order model leads to a substantial enhancement in the degree of agreement, while the third-order model offers a marginally superior fit across the entire strain range. However, given the satisfactory level of accuracy exhibited by the second-order model in its reproduction of the observed experimental behaviour, it was selected for further analysis in order to maintain a simpler and more efficient computational formulation. Subsequent to this selection, the second-order model was validated in LS-DYNA. The results, presented in Fig. 4.2b, demonstrated that the simulation produced results identical to those obtained from the analytical model.

The optimized parameters for the first-, second-, and third-term Ogden models, as well as for the General Hyper-elastic material model under quasi-static conditions, are presented in Table 4.1 .

Table 4.1: Optimized parameters for Ogden and General Hyper-elastic models at 0.01/s.

(a) Ogden Model μ [kPa], α [-]

Ogden Model	**Parameter**	**Value**
First-order	α	10.3604
	μ	0.3529
Second-order	α_1	10.3604
	μ_1	0.2053
	α_2	10.3604
	μ_2	0.1476
Third-order	α_1	10.3604
	μ_1	0.3529
	α_2	1.0361
	μ_2	0
	α_3	1.0355
	μ_3	0

(b) General Hyper-elastic Model C_i [MPa]

Hyper-elastic Model	**Parameter**	**Value**
First-order	C_{01}	0.72
	C_{10}	0
Second-order	C_{01}	0.000355
	C_{10}	0
	C_{11}	0.000639
Third-order	C_{01}	0
	C_{10}	0.000130
	C_{11}	0
	C_{20}	0.001350

4.2 Calibrated and Validated Visco-Elastic Parameters for General Hyper-Elastic and Ogden Models

The stress-strain response for a strain rate of 90/s was calibrated against experimental data for the same strain rate. This was achieved by adding the visco-elastic stress to the already fitted quasi-static stress expression, as outlined in Section 2.3. The resulting visco-elastic parameters are presented in Table 4.2 for both the Ogden and Hyper-elastic rubber models. The corresponding curves are shown in Fig. 4.3a below. Additionally, the material constants for the quasi-static Ogden and Hyper-elastic models, along with the visco-elastic parameters, were verified in LS-DYNA, as seen in Fig. 4.3b.

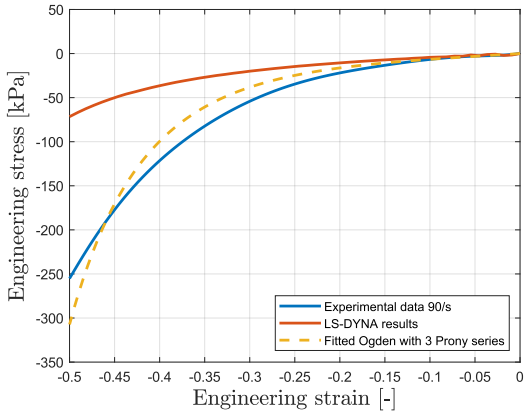

(a) Ogden model vs experimental data at 90/s

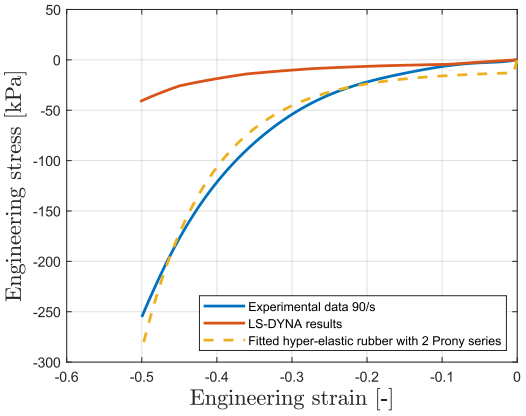

(b) Hyper-elastic model vs experimental data at 90/s

Fig. 4.3: Calibrated and validated viscous parameters versus experimental data for strain rate 90/s

It can be observed that the stress from the calibrated curve follows the experimental data fairly well up to higher strains. However, the LS-DYNA result does not align with either the experimental data or the fitted analytical curve.

Table 4.2: Fitted Prony series parameters for a strain rate of 90/s.

(a) Ogden Model g_i [kPa], β_i [1/s]

Prony Series	Parameter	Value
Series 1	g_1	0.00123
	β_1	1×10^{1}
Series 2	g_2	0.0000963
	β_2	1
Series 3	g_3	11.00790
	β_3	1×10^{-1}

(b) Hyper-elastic Rubber g_i [kPa], β_i [1/s]

Prony Series	Parameter	Value
Series 1	g_1	1.173
	β_1	1.00×10^{2}
Series 2	g_2	10.000
	β_2	1.00×10^{1}

4.3 Parameter optimization results using LS-OPT tested in SET

Two alternative sets of optimized parameters were obtained using LS-OPT, as shown in Tables 4.3 and 4.4. The method used to derive these parameters is described in Section 3.1.2.

Table 4.3: Optimized parameters for Ogden model Alternatives 1 and 2.

(a) Ogden Model Alternative 1: μ [GPa], α [-]

Ogden Model	Parameter	Value
First-order	α_1	18.14
	μ_1	5.09×10^{-8}

(b) Ogden Model Alternative 2: μ [GPa], α [-]

Ogden Model	Parameter	Value
First-order	α_1	18.37
	μ_1	1.0×10^{-7}

Table 4.4: Fitted Prony series parameters for the different alternatives.

Ogden Model Alternative 1: g_i [GPa], β_i [1/ms]

Prony Series	Parameter	Value
Series 1	g_1	2.72×10^{-6}
	β_1	1×10^{-3}
Series 2	g_2	2.17×10^{-5}
	β_2	1×10^{-2}
Series 3	g_3	1.68×10^{-5}
	β_3	10^{-1}
Series 4	g_4	1.19×10^{-6}
	β_4	1
Series 5	g_5	2.71×10^{-6}
	β_5	1×10^{1}

Ogden Model Alternative 2: g_i [GPa], β_i [1/ms]

Prony Series	Parameter	Value
Series 1	g_1	3.4×10^{-5}
	β_1	0.051
Series 2	g_2	4.83×10^{-6}
	β_2	0.137
Series 3	g_3	1.0×10^{-6}
	β_3	8.13

The two different sets of optimised parameters for the Ogden material model were implemented in the SET and then compared against experimental data at three different strain rates, as shown in Fig. 4.4.

In addition, the volume change was monitored until LS-DYNA solver termination in order to benchmark the models stability when implemented in both the Single-Element Fig. 4.5a and the Unit Cell Fig. 4.5b. The results are presented in Fig. 4.5 and benchmarked against average adipose tissue material model [15]. For the UC in Fig. 4.5 the strain is based of Eq. 3.2 and the normalised volume is the summation of volume change inside all the elements.

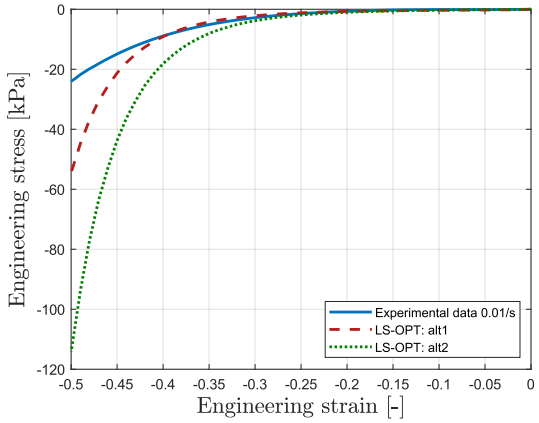

(a) Strain rate 0.01/s

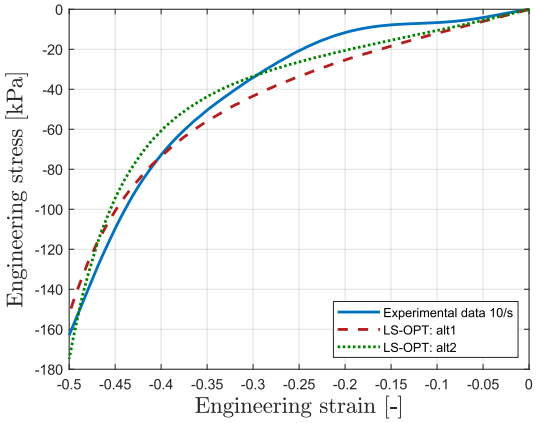

(b) Strain rate 10/s

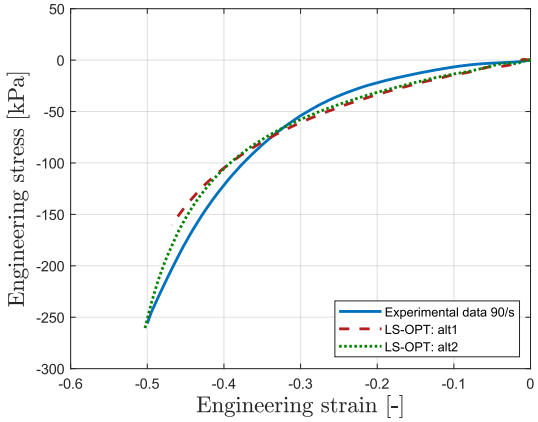

(c) Strain rate 90/s

Fig. 4.4: Optimized parameters for the Ogden model using LS-OPT compared to experimental data for various strain rates.

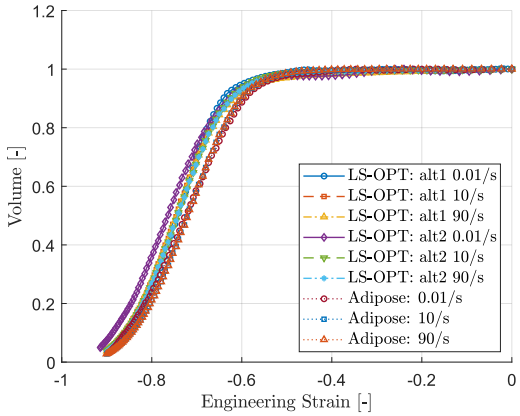

(a) Single Element volume change comparison shown against the engineering strain.

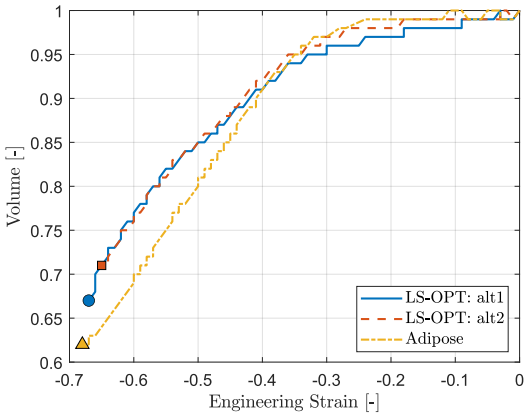

(b) Unit Cell strain limit in accordance with Eq. 3.2 for 90/s strain rate.

Fig. 4.5: Comparison of strain limit and volume change for different material models.

4.4 Result from SAFER HBMs Impact

This section presents the results from the SAFER humerus plate and bar impact along with the experimental results.

4.4.1 Humerus Plate Impact

In Fig. 4.6a and Fig. 4.6b the optimised material model parameters from Tab. 4.3 along with the Adipose Soft and Adipose Stiff from [15] are shown against the experimental data reported in [20].

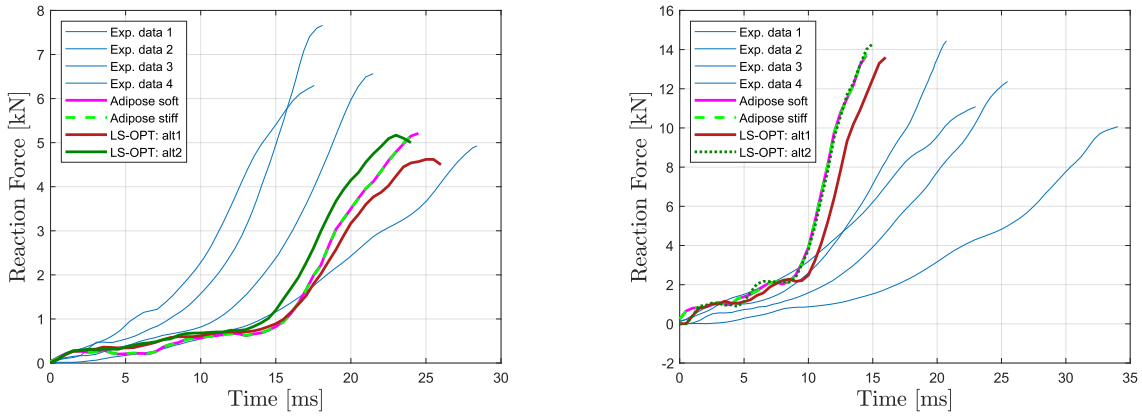

(a) 2 m/s impact.

(b) 4 m/s impact.

Fig. 4.6: Comparison of force response at different impact velocities.

It can be observed that both alternatives do not deviate significantly from each other and appear to follow a similar trend and path as the other sourced data. One noteworthy observation is that LS-OPT Alt. 2 is almost identical to the adipose soft and adipose stiff curves shown in Fig. 4.6b.

4.4.2 Humerus Bar Impact

The results from the humerus simulation in Section 4.4.1 are compared to the experimental curves from physical impact tests on female humerus cadavers from Duma et al. [21]. It is shown in Fig. 4.7, that all simulations has a delayed response in comparison to the experimental tests.

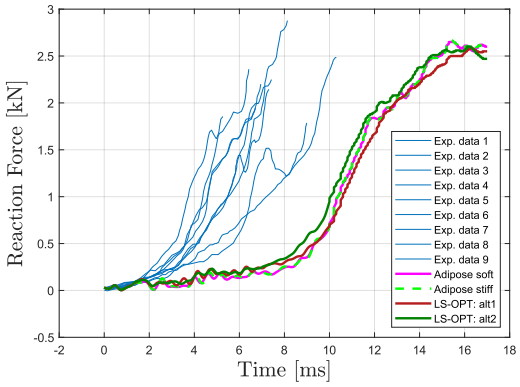

Fig. 4.7: Reaction force vs time between simulations and experimental data.

5

Discussion

In this chapter, the results obtained from the analytical and numerical simulations will be discussed. The chapter also includes discussions about limitations, errors and future work.

5.1 Material Models result

The following section is dedicated to the presentation of the material models' results, accompanied by a thorough analysis and critical evaluation. The analytical implementation of the quasi-static case demonstrated strong agreement with both experimental data and LS-DYNA simulations for the two material models, thereby suggesting that the formulation is reliable under low strain-rate conditions. However, substantial discrepancies were observed in the visco-elastic implementation for both models. The analytical model was unsuccessful in reproducing the LS-DYNA results, thereby complicating the accurate capture of the material response under time-dependent loading conditions.

These discrepancies may be ascribed to misinterpretations of the visco-elastic constitutive equations or to limitations in the overall approach employed to describe rate-dependent behaviour. Consequently, the analytical model proved inadequate in adequately representing the anticipated material response, thereby diminishing its efficacy as a verification tool for LS-DYNA simulations.

Despite this, LS-OPT successfully identified material parameters that allowed the Single-Element model to match experimental results across both quasi-static and visco-elastic regimes over varying strain rates. The analytical model proved valuable as an initial estimate for the LS-OPT parameter identification process.

A study of the strain limit and volume change in both the unit cell and single-element simulations, as illustrated in Fig. 4.5, reveals that the LS-DYNA implementation manifests stability characteristics that are in accordance with the benchmark behaviour of adipose tissue. This lends further credence to the validity and practical usefulness of the calibrated material model in capturing the mechanical response of soft biological tissues.

5.2 HBM response

A discussion regarding the SAFER HBMs impact results.

5.2.1 Humerus Plate Impact

The material models presented in 4.3, for the quasi-static case (and to some extent even at higher strain-rates) exhibit a higher stress-strain response than that of the actual test when subjected to high compressive strains, as shown in Fig. 4.4. The optimization process allows the curves to remain aligned up to a certain compressive strain, after which the material model becomes significantly stiffer than the experimental one. This behavior becomes more pronounced as the strain rate approaches the quasi-static case, as illustrated in Fig. 4.4a, compared to Fig. 4.4b and 4.4c at high compressive strains.

A comparison of the plate impact response for the two initial velocities shows that, overall, the simulation and experimental results correlate quite well for both initial ve-

locities, as shown in Fig. 4.6a-4.6b. In the 2 m/s case, the response aligns closely with the experimental data. The two proposed material models, LS-OPT: Alt1 and -Alt2, correspond to a stiffer and softer response, respectively, compared to the adipose material models from [15]. For the 4 m/s case, the model overestimates the stiffness in comparison to the experimental data. It is suspected that as the impactor slows down from its initial high velocity, the strain rate decreases (slower strain rate) while the material is subjected to high compressive strain. At this point, as discussed in the previous paragraph, the model should be stiffer than the experimental data (see Fig. 4.4). This may also explain why the 2 m/s response remains closer to the experimental data, as the impactor does not reach as high compressive strains where the material model deviates more from the experimental data. However, whether this is the true cause has not been studied.

5.2.2 Humerus Bar Impact

It can be seen that the model does not capture the experimental results well in Fig. 4.7. However, it should be noted that the stiffest responses are similar, despite the time-front offset. Overall, the simulation results do not correlate well with the experiments from [21]. Several factors could contribute to this discrepancy. The muscle specimen from which the experimental values were extracted, and to which the material data was calibrated in [11], may not be representative of the muscle used in the tests conducted by [21]. Additionally, the SAFER HBM model [19] might inaccurately represent the physical test, such as having a higher fat-to-muscle ratio, which would result in a softer response.

Given the experimental results from [21], the different outcomes compared to the HBM model could stem from the cadavers used in the testing, which may have contained less adipose tissue than the HBM model. The first soft response (at $t \in [0, 8]$ [ms]) in the simulations, as seen in Fig. 4.7, corresponds to the impactor penetrating the fat, while the second, stiffer response (at $t \in [8, 16]$ [ms]) occurs as the muscle begins to bear load. In the cadavers, if the body fat was low, the "early" stiffness observed in the experimental data could be explained.

5.2.3 Time-Zero Correlation

Regarding the results shown in Fig. 4.6 and 4.7 there are uncertainties where the initial impact (time-zero) is defined. A major uncertainty is from the experimental tests where it is harder to correlate the time-zero than it is in a numerical simulation. Specifically, looking at Fig. 4.7 with the experimental results from Duma et al. [21] which is an older study, it is suspected that the time-zero or initial contact might not be equal. It is possible that the instrumentation did not get an accurate read or too low of a response on the initial phase and the authors focused on the stiffer response. This leaves some uncertainties related to the correlation, but it can still be seen that the stiff response is closely related despite the time-axis offset.

5.3 Limitations

Several limitations were encountered during the project that affected both the modelling and optimization processes. One major limitation was the lack of access to LS-DYNA's source code, which made it difficult to fully understand the numerical implementation of the visco-elastic models. Without insight into the underlying assumptions, simplifications, or numerical methods used in LS-DYNA, explaining the differences between the analyt-

ical model and the simulation results becomes challenging. This lack of transparency particularly impacted the interpretation of the visco-elastic model's behaviour.

An isotropic material response was used for all material models, with the representative response being that of the muscle's transverse direction.

Another limitation was related to the availability of reference material. Although earlier work using QLV modelling exists, many of these sources did not clearly describe how the constitutive equations were derived or what assumptions were made, making it difficult to adopt those approaches to the specific conditions and needs of this project.

Additionally, the optimization setup presented its own challenges. The version of LS-OPT (7.0) used in this project could not be installed on Chalmers's computers and had to be run on a personal computer instead. Furthermore, only the free student version of LS-DYNA was available, which limited the solver to running a single job at a time. This significantly increased the total optimization time and reduced the efficiency of parameter fitting.

Another limitation was the time constraint caused by difficulties encountered while implementing the Ogden model in LS-OPT and integrating it into the HBM. As a result, the General Hyper-elastic model was not included in this part of the study. If addressed in future work, this model could provide a new perspective or offer a less computationally demanding method for generating material parameters for soft tissues.

5.4 Errors

Several sources of potential error were identified throughout the project, both in data processing and model implementation.

The experimental data for the compressive test of muscle was obtained from X. Zhai [11], where the stress-strain data was presented in graphical form. Since no raw data was provided, values were extracted from the graph using the WebPlotDigitizer tool (automeris.io) [22]. With this tool, the user manually defines the x and y axes and selects points along the curve to generate numerical data. Potential errors can arise from inaccuracies during point selection, as well as from limitations in image resolution and screen quality, which may affect the precision of the extracted values.

Additionally, errors may have occurred during the implementation of the analytical models in Excel. The constitutive equations were coded manually, and mistakes in the formulas, parameter handling, or cell references could have introduced errors in the results. These types of errors are difficult to detect without independent verification and may have contributed to mismatches between the analytical and numerical results.

When optimizing values in LS-OPT, the initial guesses and the acceptable parameter search ranges are crucial for finding the optimized parameters. Poor initial guesses can lead to the identification of an unsought local optimum rather than the global optimum.

5.5 Future Work

Several opportunities exist to expand upon the findings of this study and further improve the reliability and applicability of muscle material modelling in the SAFER [19] HBM framework.

One key area for future research is the development of a more accurate formulation or correlation for the viscous behaviour of the Ogden model in LS-DYNA. Establishing a clearer link between the analytical representation of viscous effects and their numerical

implementation could improve the agreement between simulation results and theoretical predictions.

Additionally, further investigation is needed into the trade-offs involved in accurately capturing high-strain-rate behaviour while potentially overestimating stresses at low strain rates. Understanding how this imbalance affects the overall response of HBM is crucial, particularly in impact scenarios where strain rates vary significantly across tissues and time.

If an analytical approach to modelling viscous effects can be robustly established, it could enable the development of predictive tools—such as a Python script—for estimating Ogden parameters. Such a tool could either serve as a independent material model predictor or be used to generate informed initial guesses for optimization routines in LS-OPT.

Another important point is the collection of additional experimental data, particularly across a wider range of strain rates and specimen types. This would support more comprehensive model calibration and validation.

Finally, running simulations with geometries that exactly match those of the experimental specimens could help reduce uncertainties related to factors like body fat-to-muscle ratio. This may also aid in validating parametrized model, such as the VIVA+ [3] model family, ensuring the models can represent a broader range of body compositions accurately.

6

Conclusion

The Ogden material model is a good fit for quasi-static conditions and smaller strain-rate ranges. The viscous part of the material however, fails to capture the non-linearity when large strain-rate ranges are required.

There is a high incentive to use LS-OPT because of the direct correlation of material model to the implementation in LS-DYNA. However, the downside is that LS-OPT is not freely available and is best utilised when reasonable initial values are known.

The viscous part in the Ogden material model implementation can capture the high strain-rate ranges, but in return overestimate the low strain-rate stress-strain response.

Ultimately, two distinct challenges arise: one in accurately modelling low strain-rate behaviour and another in representing the non-linear response under high strain-rate conditions. Until a unified model is developed that can capture both with minimal compromise, the choice of model calibration must depend on the specific simulation context and the desired outcome.

The full HBM in this study is simulated under both bar and plate impact scenarios and compared to experimental data under similar dynamic loading. Given that the primary application of this model is in automotive crash simulations, where high strain rates are common, it is essential to calibrate the model to perform reliably under such conditions. While capturing accurate behaviour across all strain rates remains challenging, prioritizing fidelity in the dynamic range relevant to crash events ensures that the model produces realistic and stable responses in full-scale simulations. This is especially critical when evaluating soft tissue deformation and injury prediction during high-speed impacts.

References

[1] OpenAI, *Chatgpt (gpt-4)*, Accessed: Mar. 28, 2025. [Online]. Available: https://chat.openai.com, 2022.

[2] J. Kutylowski, *Deepl translator*, Accessed: Mar. 28, 2025. [Online]. Available: https://www.deepl.co 2017.

[3] V. Documentation. "Vivaplus documentation." Accessed: Mar. 28, 2025. [Online]. Available: https://vivaplus.readthedocs.io/en/latest/. (2024).

[4] L. Pan. "The evolution of the crash test dummy." Accessed: Mar. 30, 2025. [Online]. Available: https://www.humaneticsgroup.com/perspectives/evolution-crash-test-dummy. (2020).

[5] J. John, C. Klug, M. Kranjec, E. Svenning, and J. Iraeus, "Hello, world! viva+: A human body model lineup to evaluate sex-differences in crash protection," *Front. Bioeng. Biotechnol.*, vol. 10, p. 918 904, 2022, Accessed: Mar. 28, 2025. DOI: 10.3389/fbioe.2022.918904.

[6] C. Dictionary. "Biomechanics." Accessed: Mar. 3, 2025. (2025), [Online]. Available: https://dictionary.cambridge.org/dictionary/english/biomechanics.

[7] B. Pipkorn, J. Iraeus, M. Björklund, *et al.*, "Multi-scale validation of a rib fracture prediction method for human body models," in *Proc. Int. Res. Council on Biomechanics of Injury (IRCOBI)*, Accessed: Mar. 28, 2025, 2019, pp. 175–192.

[8] R. Chavan, N. Kamble, C. Kuthe, and S. Sarnobat, "On mechanical behavior and characterization of soft tissues," *Biomed. Eng. Comput. Biol.*, vol. 15, p. 11 795 972 241 294 115, 2024. DOI: 10.1177/11795972241294115.

[9] E. Karabelas, M. A. F. Gsell, G. Haase, G. Plank, and C. M. Augustin, "An accurate, robust, and efficient finite element framework with applications to anisotropic, nearly and fully incompressible elasticity," *Comput. Methods Appl. Mech. Eng.*, vol. 394, p. 114 887, 2022. DOI: 10.1016/j.cma.2022.114887.

[10] LS-Dyna, *Ls-dyna r12 keyword manual vol ii*, Accessed: Mar. 28, 2025. [Online]. Available: https://lsdyna.ansys.com/manuals/, 2020.

[11] X. Zhai *et al.*, *Mechanical response of human muscle at intermediate strain rates*, Accessed: Mar. 28, 2025, 2019.

[12] I. ANSYS, *Ls-dyna theory manual*, Accessed: Mar. 28, 2025. [Online]. Available: https://lsdyna.ansys.com/manuals/, 2025.

[13] LS-Dyna, *Ls-dyna r12 keyword manual vol i*, Accessed: Mar. 28, 2025. [Online]. Available: https://lsdyna.ansys.com/manuals/, 2020.

[14] Y. Wang, K. L. Marshall, Y. Baba, E. A. Lumpkin, and G. J. Gerling, "Compressive viscoelasticity of freshly excised mouse skin is dependent on specimen thickness, strain level and rate," *PLoS ONE*, vol. 10, no. 3, e0120897, 2015. DOI: 10.1371/journal.pone.0120897.

[15] H. Naseri, *Calibration of adipose tissue material properties in ls-dyna*, Accessed: Mar. 28, 2025, 2022.

[16] J. S. Arora, "Generalized reduced gradient method," in *Introduction to Optimum Design*, 3rd, Accessed: Apr. 25, 2025., Academic Press, 2012, ch. 13.5.3. [Online]. Available: https://www.sciencedirect.com/topics/engineering/reduced-gradient.

[17] DynaSupport, *Negative volume in soft materials*, Accessed: May 15, 2025. [Online]. Available: https://www.dynasupport.com/howtos/material/negative-volume-in-soft-materials, n.d.

[18] S. Pelschus and A. Wagner, "Populations of validated and robust passive hbms," OSCCAR Project — FUTURE OCCUPANT SAFETY FOR CRASHES IN CARS, Deliverable D3.1, version 1.0, 2021, Final version. Funded by the EU Horizon 2020 programme under grant agreement No 768947. Accessed: Apr. 24, 2025. [Online]. Available: https://www.osccarproject.eu.

[19] SAFER Vehicle and Traffic Safety Centre. "Safer vehicle and traffic safety centre at chalmers." Accessed: May 20, 2025. [Online]. Available: https://www.saferresearch.com/. (2025).

[20] A. R. Kemper, "Response corridors for the medial–lateral compressive stiffness of the human arm: Implications for side impact protection," *Accid. Anal. Prev.*, vol. 50, pp. 272–280, 2013. DOI: 10.1016/j.aap.2012.04.014.

[21] S. M. Duma, P. H. Schreiber, J. D. McMaster, J. R. Crandall, C. R. Bass, and W. D. Pilkey, "Dynamic injury tolerances for long bones of the female upper extremity," *J. Anat.*, vol. 194, no. 3, pp. 463–471, 1999. DOI: 10.1046/j.1469-7580.1999.19430463.x.

[22] A. Rohatgi, *Webplotdigitizer*, Accessed: Mar. 28, 2025., 2010. [Online]. Available: https://automeris.io/WebPlotDigitizer.